Electronic, phonon and thermoelectric properties of RbLaGe half-Heusler alloy: A DFT study including spin-orbit coupling

K. Talbi[a,b], F. Khelfaoui[b,c], Y. Al-Douri[d,e,f,*], B. Bouhadef[a,b], Y. Cherchab[a,g], A. Slamani[a] and A. Bouhemadou[h]
[a] *Department of Physics, University of Relizane, Po Box 048000, Bormadia-Relizane, Algeria.*
[b]*Laboratoire De Physique Des Plaques Minces Et Technologies Avancées, Relizane,Algeria.*
[c]*Laboratory of physico-chemical studies, University of Saida- Dr. Moulay Tahar, Saida, Algeria.*
[d]*College of Health and Medical Techniques, Al-Bayan University, Baghdad, Iraq.*
[*] *yaldouri@yahoo.com*
[e]*Department of Mechanical Engineering, Faculty of Engineering,*
Piri Reis University, EflatunSk, No:8, 34940 Tuzla, Istanbul, Turkey.
[f]*Nanotechnology and Catalysis Research Centre, University of Malaya,*
50603 Kuala Lumpur, Malaysia.
[g]*Laboratoire de Microphysique et de Nanophysique (LaMiN), ENPO, Po Box 1523 EL M'Naouer,*
Oran 31000, Algeria.
[h]*Laboratory for Developing New Materials and their Characterizations, Department of Physics, Faculty of Sciences,*
Ferhat Abbas University - Setif 1, 19000 Setif, Algeria.

Received 10 January 2025; accepted 18 March 2025

The phonon, electronic and structural properties of the novel RbLaGe half-Heusler alloy are analysed using density functional theory (DFT) with the generalized gradient approximation (GGA). The semiclassical Boltzmann transport theory under the constant relaxation time approximation is employed specifically to evaluate the thermoelectric properties. The results reveal that RbLaGe is energetically, structurally, and dynamically stable, suggesting its potential for experimental synthesis. RbLaGe exhibits semiconducting behaviour with a direct bandgap, 0.79 eV. Spin-orbit coupling has a more pronounced effect on the conduction band other than on the valence band, leading to a splitting of 0.01 eV approximately at point X. Thermoelectric properties, including power factor (PF/τ), merit figure (ZT), electronic thermal conductivity (κ_e/τ), electrical conductivity (σ/τ) and Seebeck coefficient, are analyzed using Boltzmann transport theory within the rigid band approximation. The results propose that RbLaGe exhibits high thermopower, which is attributed to the flat band near the Fermi level. Furthermore, the power factor (PF) shows a strong temperature dependence, reaching a maximum value,9.9×10^{11} W/mK^{2}s at 900 K. The calculated thermal conductivity of the lattice (κ_L) reveals a significant temperature-dependent reduction, improving the merit thermoelectric figure (ZT). Incorporating spin-orbit coupling (SOC) further improves ZT by optimizing the electronic transport properties.

Keywords: DFT; half-Heusler; stability; electronic; thermoelectric.

DOI: https://doi.org/10.31349/RevMexFis.72.020502

1. Introduction

Advanced materials with unique electronic, thermoelectric and optical properties have garnered an increasing attention for their applications in energy conversion, optical communication technologies [1,2] and thermoelectric devices [3]. The ternary half-Heusler alloys (XYZ) exhibit several novel properties, including good optical absorbance [4,5], high figure of merit [6-8], half-metallicity and potential for spintronic applications [9-12]. These alloys are a promising class of non-toxic, relatively abundant and low-cost thermoelectric (TE) materials, meeting the criteria for economically viable and environmentally friendly solutions [13]. Half-Heusler alloys stand out as highly promising [13] thermoelectric materials for waste heat recovery at medium to high temperatures. Significant research has been devoted to these compounds, largely due to their remarkable thermoelectric properties [14]. In these structures, minimizing point defects can substantially enhance performance by reducing electron-acoustic phonon interactions, which help approach the theoretical limits for the power factor and achieve record-high ZT values in the temperature range, 300-873 K [15].

Moreover, electron-acoustic phonon interactions can be directed toward high mobility through symmetry-protected orbital interactions, and this regime enables large power factors in half-Heusler, significantly exceeding the maximum measured values [7]. The efficiency of thermoelectric (TE) device depends on its electrical and thermal transport properties, quantified by the dimensionless figure of merit,$ZT = (S^2\sigma T)/(\kappa_e + \kappa_l) = (S^2\sigma T)/\kappa$, where S represents Seebeck coefficient, σ is electrical conductivity and κ is total thermal conductivity, which is the sum of electronic (κ_e) and lattice (κ_l) contributions, all are evaluated at absolute temperature (T). A material's power factor, determined by the combination of its electrical conductivity and Seebeck coefficient, indicates how effectively it can generate electricity when exposed to temperature gradients.

Many half-Heusler (HH) alloys have been identified as promising candidates for thermoelectric applications due to their favourable electronic and thermal properties. Additionally, a selected few is strongly recommended for further investigation [6]. A comprehensive computational analysis of TE compounds and doped TE alloys, $Nb_{1-x}Ti_xFeSb$ has revealed that the figure of merit reaches a maximum value, $ZT \approx 0.86$ at temperature, $\sim$ 1000 K and relatively high carrier densities, $\sim 10^{21}$ cm^{-3}, closely matching experimental results [16]. Furthermore, high ZT ($\approx$ 1, at 873 K) is observed for $Zr_{1-x}Nb_xNiSn$ ($x = 0.03$), attributed to the synergistic enhancement of the power factor coupled with a reduction in thermal conductivity [17]. By engineering point defects in $Nb_{0.55}Ta_{0.40}Ti_{0.05}FeSb$, a power factor of 78 μW cm^{-1} K^{-2} is achieved, which is close to close to the theoretical prediction for the NbFeSb single crystal [15]. To enhance ZT through a drastic reduction in thermal conductivity, Rogl *et al.* [18,19] have investigated the influence of severe plastic deformation through high-pressure torsion. 8-electron half-Heusler alloys represents another class for ZT close to 1. The ZT of half-Heusler materials is approximately 1 in the temperature range $500 - 1000$ K [3,20,21]. Investigations of the CoTiSi and CoHfSi half-Heusler alloy [22,23] have demonstrated their potential for thermoelectric applications, revealing a stable structure, indirect band gaps, and enhanced Seebeck voltage, particularly for p-type doping. These findings highlight the importance of doping strategies and electronic structure tuning to achieve superior thermoelectric performance. Experimental studies have demonstrated that incorporating metallic phase nanoscale inclusions as dopants and adjusting the valence electron count can significantly enhance the Seebeck coefficient [23]. Vikram *et al.* [24] have calculated ZT = 1.37 for RbPBa and ZT = 1.56 for AgPMg. Cifitci *et al.* [25] have demonstrated that KScX (with X=C and Ge) half-Heusler are considered thermoelectrically efficient materials, with performance 1.5 times higher than Bi_2Te_2 at room temperature. Cherchab *et al.* [26] have researched KLaX (X= C, Si, Ge, and Sn) half-Heusler compounds and observed high thermopower values. Including the spin-orbit coupling (SOC) in the calculations increases the flatness of valence band from X = Si to Sn. However, the bandgap energies are affected by SOC, which is suspected to cause a downshift in the fundamental bandgap [27].

It is important to note that magnetism, even in non-magnetic materials, can significantly influence the electronic structure. This arises from interactions such as spin-orbit coupling and exchange interactions, which can affect the energy levels of electrons and their spin dynamics. Consequently, defining a spin quantization axis is a crucial for accurate calculations, not only in magnetic materials but also in systems where the magnetic moments are not aligned (non-collinear magnetism).

This work explores the structural, dynamical, electronic and thermoelectric properties of RbLaGe, a novel half-Heusler within the group I-II-IV. It is aimed to assess the feasibility of synthesizing this material experimentally to demonstrate its structural and dynamical stability. Additionally, its potential as a candidate for thermoelectric generator applications by analysing its power factor is investigated. This study is the first comprehensive investigation of the structural properties, lattice stability, thermoelectric characteristics and the impact of spin-orbit coupling (SOC) in RbLaGe half-Heusler alloy. Rb is specifically selected for this study due to its unique atomic properties, including a larger ionic radius and lower electronegativity, which is expected to significantly influence alloy stability and electronic behavior. Furthermore, the absence of prior research on Rb-based half-Heusler alloys underscores the novelty and significance of this work, which addresses a notable gap in the existing literature. The manuscript is organized as follows; Sec. 2 details the computational method, Sec. 3 represents the results and discussion, and Sec. 4 outlines the conclusions.

2. Computational method

The structural and electronic characteristics of the half-Heusler alloy RbLaGe are examined using density functional theory (DFT) with the generalized gradient approximation (GGA) [28]. The exchange-correlation energy is described using the Perdew-Burke-Ernzerhof (PBE) functional within the generalized gradient approximation (GGA) [29]. Additionally, the modified Becke-Johnson (mBJ) potential [30-33] is employed to achieve a more accurate estimation of the band gap and band structure. Due to the semi-empirical nature of the mBJ potential, the lattice parameter was optimized first using GGA. This optimized parameter is used in subsequent calculations to determine the band structure [30].

The WIEN2k package, based on the Full Potential-Linearized Augmented Plane Wave (FP-LAPW), is utilized for the optimization process [34]. The maximum angular momentum quantum number for the expansion of wave functions inside the atomic spheres is set to $l_{\max} = 10$. The parameter $R_{MT}k_{\max} = 9$ is used, where R_{MT} is the smallest atomic sphere radius within the unit cell, and $k_{\max}$ is plane-wave cutoff. Additionally, the Fourier expansion of charge density is truncate at $G_{\max} = 14Ry^{1/2}$. These calculations are performed using $17 \times 17 \times 17$ Monkhorst-Pack mesh for the Brillouin zone sampling [31].

During the self-consistency cycles, we have employed an energy convergence criterion, 0.00001 Ry and charge convergence threshold, 0.0001 e. The semiclassical Boltzmann transport theory [35], as implemented in the BoltzTrap code [36], which is used to calculate the thermal transport properties. The Seebeck coefficient (S), electrical conductivity (σ), electronic thermal conductivity (κ_e) and power factor (PF) are among the key transport properties that need to be computed as function of temperature, chemical potential and carrier concentration. For these computations, a dense $43 \times 43 \times 43$ k-point grid is generated using the Monkhorst-Pack method. The phonon dispersion curves are obtained using the Phonopy code [37], which utilizes a real-space interatomic force constant matrix derived from the computed dynamical matrices on a coarser $5 \times 5 \times 5$ q-point mesh grid.

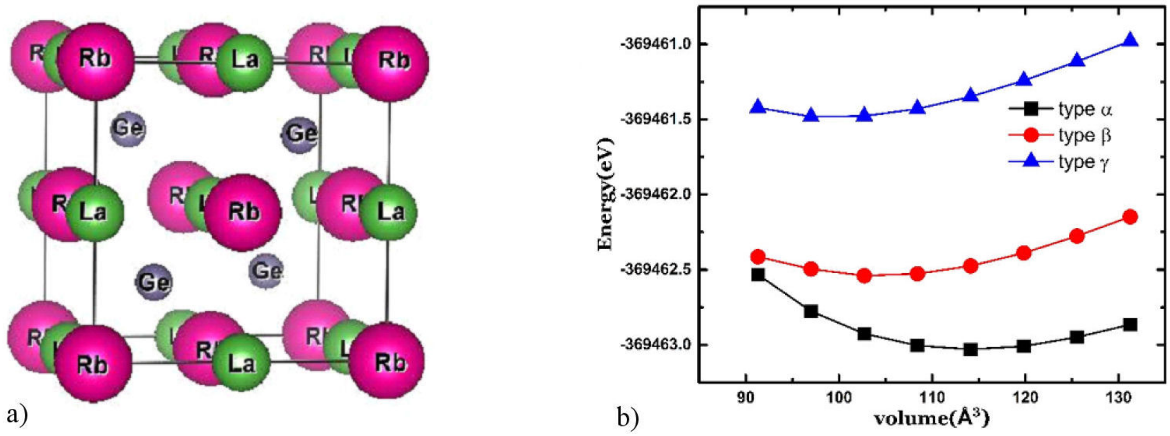

FIGURE 1. a) Total energy versus volume of RbLaGe in three phases, b) crystal structure of RbLaGe.

Due to the presence of heavy elements, the spin-orbit coupling (SOC) effect is expected to be significant in this material. Therefore, we have employed the second-variational method to include SOC in our calculations [38].

3. Results and discussions

3.1. Phase stability and lattice dynamical properties

Half-Heusler alloys exhibit three distinct configurations; α, β and γ. All crystallize in the face-cantered cubic (fcc) structure with space group, F43m (N° 216). In the α-phase of RbLaGe, Rb, La, and Ge occupy the 4a (0,0,0), 4b (1/2, 1/2,1/2), and 4c (1/4,1/4,1/4) Wyckoff positions, respectively. The β and γ phases are formed by exchanging the occupation sites of Rb and Ge, and La and Ge, respectively. The α phase is predicted to be the most stable ground state among the α, β and γ phases as illustrated in Fig. 1. To isolate and investigate the intrinsic structural and electronic properties, all calculations are performed within the non-magnetic (NM) framework, excluding the influence of magnetism. This approach provides a suitable baseline for understanding the fundamental characteristics of RbLaGe half-Heusler alloy.

The energy-volume $E(V)$ curves for the RbLaGe half-Heusler alloy are fitted using Murnaghan's equation of state [39]. This fitting procedure yielded key equilibrium parameters, including the bulk modulus (B), its pressure derivative (B'), equilibrium total energy (E_{tot}), and ground-state lattice parameter (a_0). The calculated values are $B = 24.98$ GPa, $B' = 3.415$, $E_{\text{tot}} = -369327.244$ eV for the primitive cell, and $a_0 = 7.69$ Å.

The phase stability of RbLaGe HH alloy is investigated by calculating its cohesive and formation energies. The formation energy (ΔH_f), a critical parameter for predicting the feasibility of experimental synthesis, is computed as [40-44]:

$$\Delta H_{\text{for}}^{\text{RbLaGe}} = E_{\text{tot}}^{\text{RbLaGe}} - \left(E_{\text{tot}}^{\text{Rb}} + E_{\text{tot}}^{\text{La}} + E_{\text{tot}}^{\text{Ge}}\right), \qquad (1)$$

where $E_{\text{tot}}^{\text{RbLaGe}}$ represents the total energy of RbLaGe alloy, while $E_{\text{tot}}^{\text{Rb}}$, $E_{\text{tot}}^{\text{La}}$ and $E_{\text{tot}}^{\text{Ge}}$ denote the ground state energies of Rubidium, Lanthanum, and Germanium, respectively. Our calculated formation energy of RbLaGe is -1.26 eV. This negative value indicates that the material potentially synthesizable experimentally and energetically stable. To further assess the structural stability and its experimental formation, the cohesive energy E_c is calculated using the following [45]:

$$E_C^{\text{RbLaGe}} = E_{\text{tot}}^{\text{RbLaGe}} - \left(E_a^{\text{Rb}} + E_a^{\text{La}} + E_a^{\text{Ge}}\right), \qquad (2)$$

where E_a represents the energy of isolated atom. For the RbLaGe half-Heusler alloy, the calculated cohesive energy (E_C) is -7.36 eV. A negative E_C value further suggests structural stability. Both the formation enthalpy and cohesive energy calculations confirm the phase's structural stability, indicating its potential for experimental synthesis under ambient conditions. Importantly, our calculated equilibrium parameters, including the bulk modulus and lattice constant are not available in the existing literature.

Furthermore, the RbLaGe half-Heusler alloy's dynamic stability is confirmed through phonon dispersion calculations using Phonopy code [37]. Figure 2 depicts the phonon dispersion curves along high-symmetry$\Gamma - X - K - \Gamma - L - X - W$

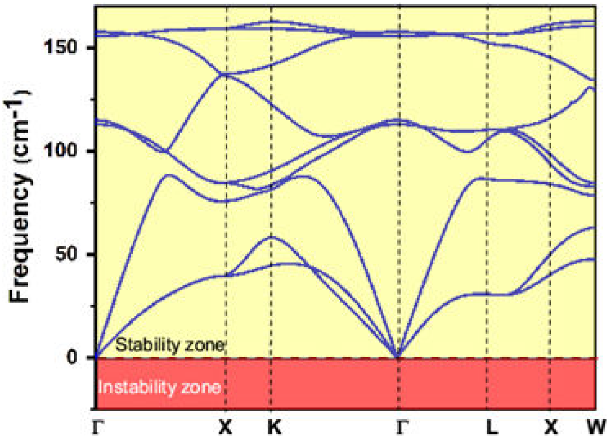

FIGURE 2. Phonon dispersion curves of RbLaGe half-Heusler alloy.

in the first Brillouin zone. The absence of any imaginary phonon frequencies in these curves confirms the dynamic stability of the RbLaGe alloy. The primitive cell contains three atoms, which give a rise to nine vibrational modes; three acoustic modes and six optical modes. Acoustic modes dominate heat transfer because of their high group velocities and strong dispersion [46]. The high acoustic frequency, found at directionΓ, is approximately 2.64 THz (88.17 cm^{-1}) , which is agreed with other half-Heusler alloys, which typically exhibit acoustic frequencies around 100 cm^{-1} [47]. The optical phonon branches exhibit a minimum frequency, 2.46 THz (81.16 cm^{-1}) along the direction X-K in Brillouin zone, resulting in an overlap with the acoustic branches. This feature is favourable for enhancing the thermoelectric performance of RbLaGe alloy by promoting strong phonon scattering and consequently reducing the thermal conductivity [48] as reported for RbYSn [27]. These findings, along with the absence of imaginary frequencies, confirm the dynamical stability of the RbLaGe alloy.

3.2. Electronic properties

The electronic properties of the RbLaGe half-Heusler alloy are investigated using the modified Becke-Jhonson exchange-correlation potential, both with and without spin-orbit coupling (SOC). To account for the influence of spin, SOC is included in the calculations of magnetic configuration with magnetization aligned along the direction [011], which is found to be the lowest-energy state as given in Table I.

This explains for the reported magnetization, which arises from SOC effects rather than spin polarization, as no ferromagnetic state is presented. The electronic band structure of the RbLaGe half-Heusler alloy is illustrated in Fig. 3, with the Fermi level set to zero zone, the band structure is computed along the high symmetry, direction W-L-Γ-X-W-K within the first Brillouin zone. Figure 3 reveals that RbLaGe exhibits a direct bandgap at the point X, with a value, 0.55 eV. When SOC is included, the bandgap slightly decreases to 0.51 eV. These results align well with previous theoretical studies on I-II-IV half-Heusler alloys [26].

A detailed analysis of the band structure, calculated using mBJ potential, reveals a localized flatness near the point X at both the valence band maximum (VBM) and conduction band minimum (CBM). Additionally, the VBM exhibits two-fold degeneracy along L-Γ-X. Furthermore, CBM exhibits two-fold degeneracy along the direction L-Γ. The flatness, associated with this degeneracy, along with the resulting large effective masses of charge carriers, is expected to enhance thermopower, as observed in Li-based half-Heusler alloys (X = Li; Y = Sc, Be; Z = Si, Ge, Bi, Sb, As) [49]. As depicted in Fig. 3, the significant impact of SOC is evident in the band structure, particularly near the VBM and CBM, where pronounced band splitting is observed. To elucidate the impact of SOC on the conduction band, we have calculated the spin-orbit splitting at the Fermi level. This significant parameter is found to be approximately 0.01 eV, which is expected to reduce the fundamental bandgap. This observation aligns with the findings of Hoat *et al*. [27], who have reported a similar decreasing in the bandgap of RbYSn from 0.892 eV to 0.825 eV due to influence of SOC.

TABLE I. RbLaGe alloy's total energy (meV) with varying magnetization directions ([001] used as reference).

Magnetization direction						
[001]	[010]	[100]	[110]	[101]	[011]	[111]
0.00	-7.57	-7.57	-7.73	-0.95	-0.92	-2.66

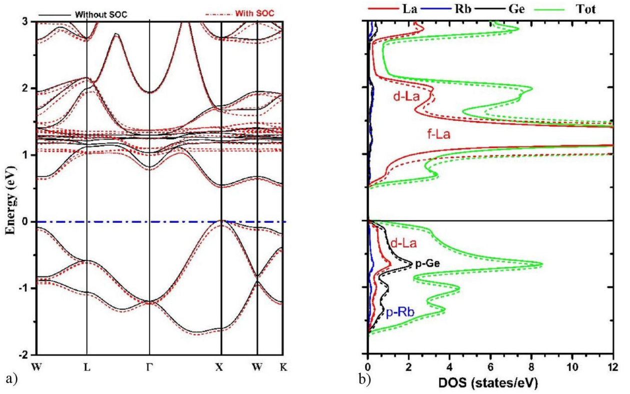

FIGURE 3. Self-consistent band structure a) and density of states b) for RbLaGe using GGA+mBJ: comparison without SOC (solid line) and with SOC (dashed line).

To gain deeper insight into the electronic structure of RbLaGe alloy, we have calculated its density of states (DOS), including the total DOS (TDOS) and partial DOS(PDOS), using the mBJ potential, as shown in Fig. 3. The figure illustrates that the valence band top near the Fermi level (E_F) is characterized by two distinct groups of sharp peaks. The first group, located closer to the VBM, primarily originates from the strong hybridization between the p-orbitals of Ge and d-orbitals of La. The second group of peaks, slightly lower in energy, originates from the same orbitals. A similar trend has been observed in other system [50]. On the conduction side, the bottom of conduction band (CB), just above E_F, is split into two sub-bands, both predominantly attributed to La atoms. The higher sub-band is dominated by a strong f-orbital contribution, while the lower sub-band primarily consists of d-orbitals. Notably, an inverse relationship between the f- and d-orbital contributions has been observed in KLaGe alloy [51].

3.3. Thermoelectric properties

The rigid band approximation, as implemented in the BoltzTraP code, is used to calculate the thermoelectric properties of RbLaGe, including the Seebeck coefficient (S), power factor (PF) and thermal conductivity (κ). These calculations are performed within the framework of semi-classical Boltzmann theory [52]. For this purpose, we have utilized Monkhorst-Pack k-point grid of $43 \times 43 \times 43$.

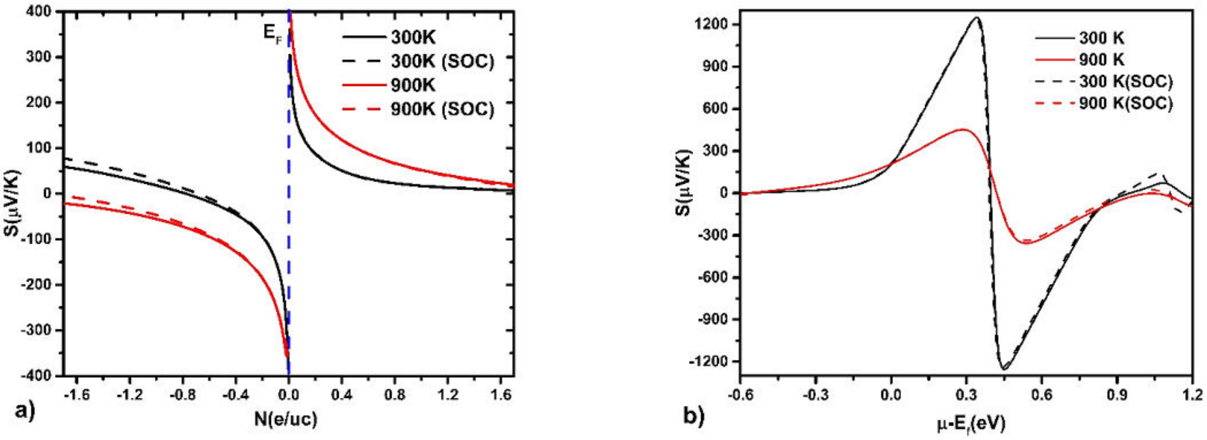

FIGURE 4. Seebeck coefficient of RbLaGe alloy with and without SOC as function of a) doping concentration and b) chemical potential at temperatures 300 K and 900 K.

These calculations are based on the constant relaxation time approximation (CRTA), which is a widely used method in computational studies to estimate the Seebeck coefficient, electrical conductivity and electronic thermal conductivity. However, it is important to note that this approach assumes a fixed relaxation time for charge carriers, independent of temperature, doping level or scattering mechanisms. While this simplification provides a useful framework for understanding the relative trends in thermoelectric performance, it does not capture the complex dependencies of relaxation time on various material-specific factors such as phonon-electron interactions, defect scattering and carrier concentrations.

To, accurately, evaluate the relaxation time, detailed studies involving first-principles calculations of scattering rates or experimental measurements are required. These factors can significantly influence the absolute values of the calculated thermoelectric properties and figure of merit (ZT). As such, the results presented in this study should be interpreted in the context of CRTA, which provides insights into the material's potential thermoelectric performance but does not account for these complex dependencies. We acknowledge this limitation and emphasize that studies incorporating relaxation time calculations or experimental validation would be necessary to provide a more comprehensive evaluation of the thermoelectric properties of the material.

Figure 4 illustrates the variation of Seebeck coefficient (S) with chemical potential and carrier concentration at temperatures, 300 K and 900 K, spanning a range from -1.6 eV to 1.6 eV. The Seebeck coefficient exhibits two prominent peaks; one in the negative region near the CBM and another in positive region near VBM. This suggests that both hole and electron charge carriers can contribute to charge transport.

As illustrated in Fig. 4a), the Seebeck coefficient (S) displays high values at lower doping concentrations but diminishes as the doping level increases. In contrast, elevating the temperature improves the thermal performance of RbLaGe alloy, highlighting its potential as a key factor in optimizing thermoelectric efficiency. For optimal thermoelectric performance, the Seebeck coefficient (S) retains a substantial value as the Fermi level approaches the band edge [53]. In the case of RbLaGe alloy, the inclusion of SOC results a slight reduction in the value, S, a behaviour that contrasts with observations reported for the RbYGe half-Heusler alloy [45].

Figure 4b) illustrates the variation of the Seebeck coefficient (S) as function of chemical potential ($\mu - E_F$) for the RbLaGe alloy at 300 K and 900 K, within the range, -0.6 eV to 1.2 eV. Two distinct peaks in the Seebeck coefficient are observed; one in the n-type region and another in p-type region. At 300 K, the peak values near Fermi level reach 1242 μV/K and -1244 μV/K for p-type and n-type doping, respectively. As temperature increases from 300 K to 900 K, a significant reduction in the maximum absolute value, S is evident. Specifically, at 900 K, the maximum Seebeck coefficient values decrease to 455(-355) (μV/K) for n(p)-type doping. These finding align with prior calculations for I-III-IV half-Heusler systems, demonstrating a similar trend in the Seebeck coefficient, as reported by Hoat *et al.* [27] for RbYSn. Additionally, S values for RbLaGe at room temperature are higher than those reported by Besbes *et al.* [54] for RbScSn.

Figures 5 and 6 depict the variations in RbLaGe's electrical conductivity (σ/τ) and electronic thermal conductivity (κ_e/τ) as functions of carrier concentration and chemical potential at 300 K and 900 K, respectively. As shown in Fig. 5a), σ/τ increases linearly up to 0.8 e/uc for hole concentration and -0.8 e/uc for electron concentration, beyond which the rate of increasing diminishes sharply. Additionally, it is evident that σ/τ decreases as temperature rises. It appears that SOC has a negligible effect on p-doping in the RbLaGe HH alloy. However, in the case of n-doping, SOC leads to a reduction in σ/τ. This decreasing can be attributed to the significant influence of SOC on the conduction band, particularly the increasing in the effective mass of electrons. This trend contrasts with the findings reported by Hoat et al. [27] for RbYSn HH alloy. As shown in Fig. 5b), σ/τ values in the electron carrier region are consistently higher than those in hole carrier region, suggesting that n-doping is more advantageous for enhancing the thermoelectric performance

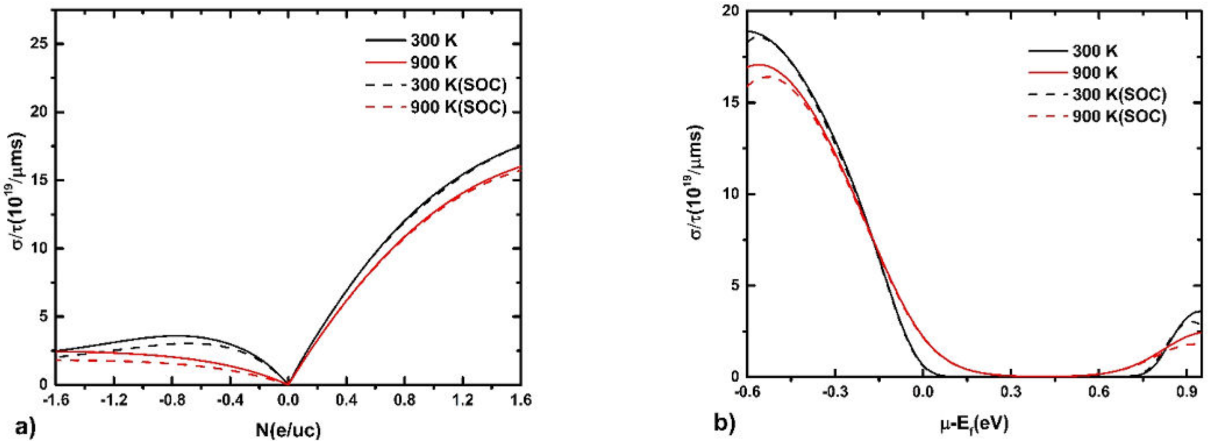

FIGURE 5. Electrical conductivity of RbLaGe alloy with and without SOC as function of a) doping concentration and b) chemical potential at temperatures 300 K and 900 K.

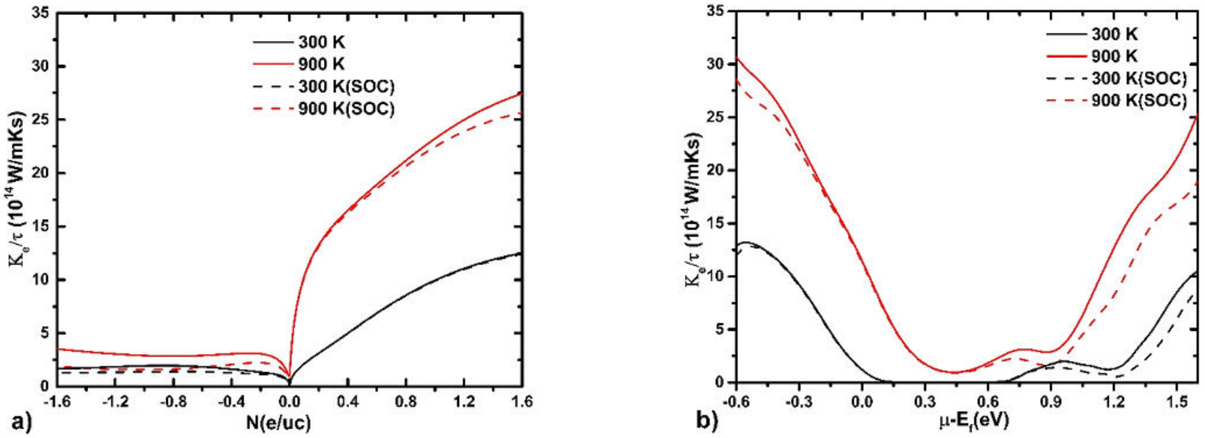

FIGURE 6. Electronic thermal conductivity of RbLaGe alloy with and without SOC as function of a) doping concentration and b) chemical potential at temperatures 300 K and 900 K.

of RbLaGe alloy compared to p-doping. However, there is no significant change is observed when SOC is included in the calculations. Without SOC, the largest values of σ/τ expected for n-type doping are 18.84×10^{19} $(\Omega\text{ms})^{-1}$ and 17.06×10^{19} $(\Omega\text{ms})^{-1}$ at temperatures, 300 K and 900 K, respectively.

Thermal conductivity (κ) consists of two primary contributions; the electronic part (κ_e) and lattice vibration part (κ_L). The BoltzTraP code specifically calculates the electronic component (κ_e/τ). Figure 6 demonstrates a strong correlation between electrical conductivity (σ/τ) and electronic thermal conductivity (κ_e/τ), consistent with the Wiedemann-Franz law [55]. This law is expressed as:

$$\kappa = \sigma \cdot L \cdot T, \tag{3}$$

where L is Lorenz number. To achieve high thermoelectric efficiency, it is a crucial to minimize the total thermal conductivity. Figure 6a) illustrates the influence of temperature and doping concentration on κ_e/τ. When electron doping is present, the inclusion of SOC reduces this parameter, whereas for hole doping, there is no significant change is observed. Within the considered chemical potential range, -0.3 eV to 0.9 eV, small values of κ_e/τ are observed, with two distinct maxima in the n-type (p-type) regions. At 300 K, the maxima are $9.13(2.95) \times 10^{14}$ (W/mK s), while at 900 K, they are 2.05 $(22.78) \times 10^{14}$ (W/mKs). The resulting κ_e/τ values are 10×10^{14} (W/Kms) and 19.1×10^{14} (W/Kms) at 300 K and 900 K, respectively. These values are slightly lower than those reported by Hoat *et al.* [27] for RbYSn in the n-region when SOC is excluded.

The thermoelectric power factor (PF) is a crucial parameter in optimizing thermoelectric materials, as it reflects the balance between the electrical conductivity (σ) and Seebeck coefficient (S) as expressed in the following:

$$PF = S^2\sigma. \tag{4}$$

Figure 7a) illustrates the dependence of the power factor (PF/τ) on the carrier concentration of RbLaGe at 300 K and 900 K. Table II displays the power factor (PF/τ) values corresponding to optimal doping levels. The results reveal that the PF/τ values are consistently higher in the hole concentration range, $0.1 - 0.4$ (e/uc) compared to the electron con-

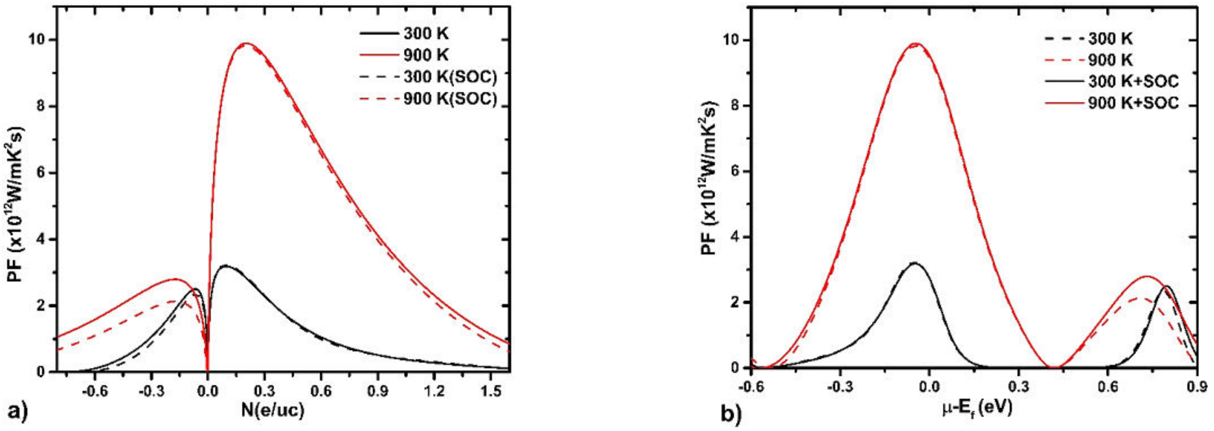

FIGURE 7. Power factor of RbLaGe half-Heusler alloy as function of a) carriers' concentration and b) chemical potential at temperatures 300 K and 900 K.

TABLE II. Maximum values of Seebeck coefficient S (μV/K); electric conductivity σ ($10^{19}/\Omega$ ms), electrical thermal conductivity κ/τ (10^{14} W/msK), and power factor PF (10^{12} W/mK^{2}s) of RbLaGe HH compound at temperatures 300 K and 900 K.

n-type				p-type			
S	σ/τ	κ/τ	$PF\tau$	S	σ/τ	κ/τ	$PF\tau$
mBJ at 300 K							
1244	18.84	13.4	2.53	1242	3.59	10.1	3.2
mBJ+SOC at 300 K							
1244	18.84	13.1	2.37	1242	3.59	8.8	3.2
mBJ at 900 K							
355	17.06	30.4	2.8	455	2.49	24.9	9.9
mBJ+SOC at 900 K							
333	16.38	28.09	2.19	455	1.76	18.6	9.9

centration range, 0.1-0.3 (e/uc). Additionally, we have compared the maximum power factor (PF) of RbLaGe with that of Half-Heusler compounds, such as FeVAs and FeVP [56], which share structural similarities with RbLaGe and are well-established in thermoelectric research.

The comparison demonstrates that RbLaGe exhibits a significantly higher power factor than both FeVAs and FeVP at 300 K. Notably, RbLaGe achieves a maximum p-type power factor of 3.2×10^{12} (W/mK^{2}s) at 900 K, which is substantially greater than the values reported for FeVAs and FeVP, which are approximately 0.35×1012 (W/mK^{2}s) for both p-type and n-type at 300 K. This suggests that RbLaGe holds considerable promise for high-temperature thermoelectric applications, potentially offering a competitive advantage over these established half-Heusler materials. Furthermore, the inclusion of SOC does not significantly alter the power factor for RbLaGe, underscoring the robustness of its intrinsic thermoelectric performance across different computational models.

Figure 7b) shows the calculated PF/τ as function of cemical potential ($\mu - E_F$) for the RbLaGe HH alloy at 300 K and 900 K. The plot exhibits two distinct peaks, with the higher peak corresponding to n-type doping and the other to p-type doping. The elevated PF values are attributed to the behaviour of band structure near to CBM and VBM, where a rapid increasing in the DOS occurs close to the band edge [57].

The power factor of the investigated material increases significantly with rising temperature. The mBJ potential predicts the highest power factor, 9.84×10^{11} (W/mK^{2}s) for p-type doping at a hole concentration, 0.196 (e/uc) or a chemical potential, -0.05 eV. In contrast, the maximum PF for n-type doping is predicted to be 2.8×10^{11} (W/mK^{2}s) at an electron concentration of, -0.16 (e/uc) or a chemical potential, 0.73 eV.

When SOC is included, the maximum PF/τ value is found to be 9.9×10^{11} (W/K^{2}ms) in the p-type doping regime, corresponding to a hole concentration, 0.2 (e/uc) and a chemical potential, -0.04 eV. Previous studies [58-60] have demonstrated that a combination of heavy and light holes is advantageous for achieving higher PF values in p-type doping. The power factor under investigation increases significantly with rising temperature, making RbLaGe a promising candidate for high temperature thermoelectric applications.

The thermoelectric performance of RbLaGe, characterized by the figure of merit (ZT), depends on the interplay between lattice thermal conductivity κ_L and electronic transport properties κ_e. The figure of merit is defined as:

$$ZT = \frac{S^2 \cdot \sigma \cdot T}{\kappa_e + \kappa_L}. \tag{5}$$

Figure 8 shows the temperature-dependent κ_L, obtained using the Slack model [61], for the studied half-Heusler alloy, both with and without spin-orbit coupling (SOC). The results indicate a significant reduction in κ_L with an increasing temperature, attributed to enhanced phonon-phonon scattering at elevated temperatures. It is important to highlight that our ZT calculations incorporate both electronic and lattice thermal conductivity contributions, ensuring a comprehensive evaluation of thermoelectric performance. While the

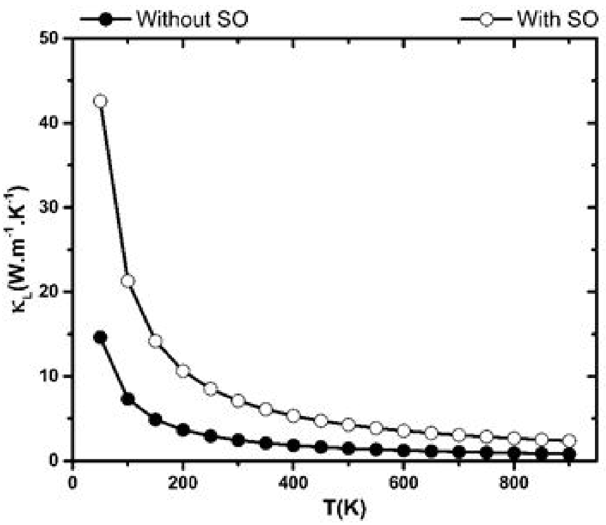

FIGURE 8. Lattice Thermal Conductivity (κ_L) of RbLaGe as a function of temperature, with and without spin-orbit coupling (SOC).

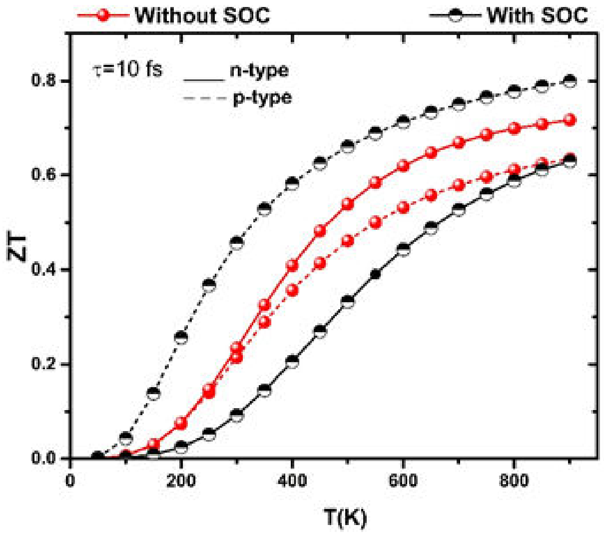

FIGURE 9. Temperature-dependent figure of merit (ZT) for p-Type and n-Type RbLaGe with and without spin-orbit coupling (SOC) Using estimated relaxation time, 10 fs.

constant relaxation time approximation (CRTA) is a simplification, it remains a widely used approach in thermoelectric studies to capture trends and relative improvements in transport properties. The presented results clearly demonstrate the role of SOC and carrier type in enhancing thermoelectric efficiency, reinforcing the significance of optimizing both electronic and lattice contributions for improved performance.

Figure 9 presents the calculated ZT for both p-type and n-type materials as a function of temperature, incorporating the κ_L values from Fig. 8. For these calculations, an estimated constant relaxation time of 10 fs is used, a typical approximation for such studies [62-64]. SOC consistently enhances ZT for both carrier types, which is attributed to SOC-induced changes in the electronic band structure, such as reduced carrier effective mass or altered scattering mechanisms, boosting the Seebeck coefficient and electrical conductivity. Additionally, the p-type materials exhibit higher ZT values than n-type materials, likely due to more favourable carrier transport properties and higher Seebeck coefficients under SOC.

In summary, the reduction in κ_L as shown in Fig. 8 is a critical for achieving high ZT values, as it minimizes thermal losses. The inclusion of SOC increases not only κ_L but also enhances the electronic transport properties, leading to improved ZTvalues, as demonstrated in Fig. 9. The using of a constant relaxation time, 10 fs in ZT calculation is a simplifying assumption, but it effectively highlights the influence of SOC and carrier type on thermoelectric performance.

The key thermoelectric parameters of RbLaGe at 300 K and 900 K are summarized in Table II. The Seebeck coefficient (S), electrical conductivity (σ/tau), electronic thermal conductivity ($\kappa_e\tau$) and power factor (PF/τ) are listed for both n-type and p-type doping, with and without the inclusion of spin-orbit coupling (SOC). Notably, the n-type configuration exhibits significantly higher Seebeck coefficients than p-type at both temperatures, with a substantial decrease at 900 K. The power factor is generally higher for p-type at 900 K, particularly when SOC effects are included, suggesting a more favourable thermoelectric performance under these conditions.

4. Conclusions

In this study, we have investigated the thermoelectric, electronic and structural properties of RbLaGe, a rare-earth-based intermetallic alloy, using the FP-LAPW method. Our findings have demonstrated that RbLaGe crystallizes in a half-Heusler structure, particularly in its $\alpha - phase$, which underpins its distinctive physical characteristics. The negative formation energy suggests that the alloy is thermodynamically stable and experimentally feasible to synthesize. Electronic structure calculations indicate that RbLaGe exhibits promising characteristics, positioning it a potential candidate for electronic and energy-related applications. Additionally, our in-depth analysis of thermoelectric properties of RbLaGe has revealed several advantageous features, further underscoring its potential for practical use. The alloy exhibits a high-power factor, especially in the n-type doping regime. The inclusion of spin-orbit coupling has a significant impact on the electronic structure and transport properties, with particularly pronounced effects observed in the p-type regime. The improvement in the thermoelectric power factor for n-type doping is primarily due to advantageous band structure near the conduction band minimum. The thermoelectric performance of RbLaGe depends on both lattice and electronic properties. While κ_L decreases with temperature, benefiting ZT, p-type and n-type variants exhibit different electronic behaviours influenced by spin-orbit coupling. These findings underscore the potential for further optimization through adjustments in carrier concentration and introduction of additional dopants, which could lead to even greater thermoelectric performance.

Acknowledgement

Y. A. would like to acknowledge Al-Bayan University for fruitful support.

Conflict of Interest

The authors declare that they have no conflict of interest.

Funding

No funding was received.

Ethical Approvals

We confirm that this work is original and has not been neither published elsewhere nor currently under consideration for publication elsewhere and has ethical issues and NO CONFLICT OF INTEREST.

Competing interests

We have no financial competing interests. We just want to explore our research productivity through this work.

Availability of data and materials

All used data is embedded in this manuscript and properly referenced where applicable.

---

1. S. Cheng, *et al.,* High sensitivity five band tunable metamaterial absorption device based on block like Dirac semimetals, *Optics Communications* **569** (2024) 130816, `https://doi.org/10.1016/j.optcom.2024.130816`
2. Z. Chen *et al.,* Ultra wideband absorption absorber based on Dirac semimetallic and graphene metamaterials, *Physics Letters A* **517** (2024) 129675, `https://doi.org/10.1016/j.physleta.2024.129675`
3. S. Chen and Z. Ren, Recent progress of half-Heusler for moderate temperature thermoelectric applications, *Materials today* **16** (2013) 387, `https://doi.org/10.1016/j.mattod.2013.09.015`
4. F. Casper *et al.,* Half-Heusler compounds: novel materials for energy and spintronic applications, *Semiconductor Science and Technology* **27** (2012) 063001, `https://doi.org/10.1088/0268-1242/27/6/063001`
5. D. Kieven *et al.,* I-II-V half-Heusler compounds for optoelectronics: Ab initio calculations, *Physical Review B-Condensed Matter and Materials Physics* **81** (2010) 075208, `https://doi.org/10.1103/PhysRevB.81.075208`
6. J. Yang *et al.,* Evaluation of half-Heusler compounds as thermoelectric materials based on the calculated electrical transport properties, *Advanced Functional Materials* **18** (2008) 2880, `https://doi.org/10.1002/adfm.200701369`
7. J. Zhou *et al.,* Large thermoelectric power factor from crystal symmetry-protected non-bonding orbital in half-Heuslers, *Nature communications* **9** (2018) 1721, `https://doi.org/10.1038/s41467-018-03866-w`
8. H. Missoum *et al.,* High ZT of new half-Heusler LiXZ (X= La, Y and Z= Ge, Si) alloys at room temperature, *Journal of Physics and Chemistry of Solids* **193** (2024) 112186, `https://doi.org/10.1016/j.jpcs.2024.112186`
9. N. A. Ganie, S. A. Mir, and D. C. Gupta, Tantalum half-Heusler alloys RbTaSi and RbTaGe: potential candidates for desirable thermoelectric and spintronic applications, *RSC advances* **13** (2023) 7087, `https://doi.org/10.1039/D3RA00146F`
10. C. J. Palmstro m, Heusler compounds and spintronics, *Progress in Crystal Growth and Characterization of Materials* **62** (2016) 371, `https://doi.org/10.1016/j.pcrysgrow.2016.04.020`
11. A. Lorf *et al.,* Structural and Half-Metallic Stabilities of the Half-Heusler Alloys KNaAs, KRbAs and NaRbAs: First Principles Method, In Spin, **vol. 11** (World Scientific, 2021) p. 2150010, `https://doi.org/10.1142/S2010324721500107.`
12. N. Marbouh *et al.,* Theoretical Prediction of Structural Stability, Electronic, Elastic, and Magnetic Properties of the New Half Metallic Half-Heusler XSrC (X= Li and Na) Alloys, In Spin, **vol. 12** (World Scientific, 2022) p. 2250027, `https://doi.org/10.1142/S2010324722500278.`
13. J. Wei, Y. Guo, and G. Wang, Exploring structural, mechanical, and thermoelectric properties of half-Heusler compounds RhBiX (X= Ti, Zr, Hf): A first-principles investigation, *RSC advances* **13** (2023) 11513, `https://doi.org/10.1039/D3RA01262J`
14. R. J. Quinn and J.-W. G. Bos, Advances in half-Heusler alloys for thermoelectric power generation, *Materials advances* **2** (2021) 6246, `https://doi.org/10.1039/D1MA00707F`
15. H. Zhu*et al.,* Half-Heusler alloys as emerging high power density thermoelectric cooling materials, *Nature communications* **14** (2023) 3300, `https://doi.org/10.1038/s41467-023-38446-0`
16. A. Hong*et al.,* Full-scale computation for all the thermoelectric property parameters of half-Heusler compounds, *Scientific reports* **6** (2016) 22778, `https://doi.org/10.1038/srep22778`
17. K. K. Johari*et al.,* High thermoelectric performance in ntype degenerate ZrNiSn-based half-heusler alloys driven by enhanced weighted mobility and lattice anharmonicity, *ACS Applied Energy Materials* **4** (2021) 3393, `https://pubs.acs.org/doi/10.1021/acsaem.0c03152.`

18. G. Rogl, M. J. Zehetbauer, and P. F. Rogl, The effect of severe plastic deformation on thermoelectric performance of skutterudites, half-Heuslers and Bi-tellurides, *Materials Transactions* **60** (2019) 2071, `https://pubs.acs.org/doi/10.2320/matertrans.MF201941`
19. G. Rogl*et al.*, Half-Heusler alloys: Enhancement of ZT after severe plastic deformation (ultra-low thermal conductivity), *Acta Materialia* **183** (2020) 285, `https://doi.org/10.1016/j.actamat.2019.11.010`
20. W. Xie*et al.*, Recent advances in nanostructured thermoelectric half-Heusler compounds, *Nanomaterials* **2** (2012) 379, `https://doi.org/10.3390/nano2040379`
21. T. Zhu*et al.*, High efficiency half-Heusler thermoelectric materials for energy harvesting, *Advanced Energy Materials* **5** (2015) 1500588, `https://doi.org/10.1002/aenm.201500588`
22. A. Shukla*et al.*, Electronic structure and thermoelectric properties of CoTiSi half-Heusler alloy: Doping overtones, *AIP Advances* **15** (2025), `https://doi.org/10.1063/5.0242686`
23. S. Matth, S. Pandey, and H. Pandey, Unravelling the effect of strain on the electronic structure, elastic and thermoelectric properties of half-Heusler alloy CoHfSi, *Physica Scripta* **100** (2024) 015928, `https://doi.org/10.1088/1402-4896/ad96f2`
24. B. Sahni*et al.*, Reliable prediction of new quantum materials for topological and renewable-energy applications: A high-throughput screening, *The Journal of Physical Chemistry Letters* **11** (2020) 6364, `https://doi.org/10.1021/acs.jpclett.0c01271`
25. Y. O. Ciftci and S. D. Mahanti, Electronic structure and thermoelectric properties of half-Heusler compounds with eight electron valence count-KScX (X= C and Ge), *Journal of Applied Physics* **119** (2016), `https://doi.org/10.1063/1.4945435`
26. Y. Cherchab and R. Gonzalez-Hernandez, Structural stability and thermoelectric properties of new discovered half-Heusler KLaX (X= C, Si, Ge, and Sn) compounds, *Computational and Theoretical Chemistry* **1200** (2021) 113231, `https://doi.org/10.1016/j.comptc.2021.113231`
27. D. Hoat and M. Naseri, Electronic and thermoelectric properties of RbYSn half-Heusler compound with 8 valence electrons: spin-orbit coupling effect, *Chemical Physics* **528** (2020) 110510, `https://doi.org/10.1016/j.chemphys.2019.110510`
28. W. Kohn and L. J. Sham, Self-consistent equations including exchange and correlation effects, *Physical review* **140** (1965) A1133, `https://doi.org/10.1103/PhysRev.140.A11330`
29. J. P. Perdew, K. Burke, and M. Ernzerhof, Generalized gradient approximation made simple, *Physical review letters* **77** (1996) 3865, `https://doi.org/10.1103/PhysRevLett.77.3865`
30. F. Tran, P. Blaha, and K. Schwarz, Band gap calculations with Becke-Johnson exchange potential, *Journal of Physics: Condensed Matter* **19** (2007) 196208, `https://doi.org/10.1088/0953-8984/19/19/196208`
31. F. Tran and P. Blaha, Accurate band gaps of semiconductors and insulators¡? format?¿ with a semilocal exchangecorrelation potential, *Physical review letters* **102** (2009) 226401, `https://doi.org/10.1103/PhysRevLett.102.226401`
32. D. Koller, F. Tran, and P. Blaha, Improving the modified Becke-Johnson exchange potential, *Physical Review B-Condensed Matter and Materials Physics* **85** (2012) 155109, `https://doi.org/10.1103/PhysRevB.85.155109`
33. M. Bouhbou *et al.*, Magnetic, half-metallicity and electronic studies of Cd1-xZnxCr2Se4 chromium selenospinels, *Journal of Magnetism and Magnetic Materials* **476** (2019) 86, `https://doi.org/10.1016/j.jmmm.2018.12.063`
34. K. Schwarz and P. Blaha, Solid state calculations using WIEN2k, *Computational Materials Science* **28** (2003) 259, `https://doi.org/10.1016/S0927-0256(03)00112-5`
35. P. B. Allen and M. Liu, Joule heating in Boltzmann theory of metals, *Physical Review B* **102** (2020) 165134, `https://doi.org/10.1103/PhysRevB.102.165134`
36. G. K. Madsen and D. J. Singh, BoltzTraP. A code for calculating band-structure dependent quantities, *Computer Physics Communications* **175** (2006) 67, `https://doi.org/10.1016/j.cpc.2006.03.007`
37. A. Togo and I. Tanaka, First principles phonon calculations in materials science, *Scripta Materialia* **108** (2015) 1, `https://doi.org/10.1016/j.scriptamat.2015.07.021`
38. D. Koelling and B. Harmon, A technique for relativistic spin-polarised calculations, *Journal of Physics C: Solid State Physics* **10** (1977) 3107, `https://doi.org/10.1088/0022-3719/10/16/019`
39. F. D. Murnaghan, The compressibility of media under extreme pressures, *Proceedings of the National Academy of Sciences* **30** (1944) 244, `https://doi.org/10.1073/pnas.30.9.244`
40. H. Alqurashi, R. Haleoot, and B. Hamad, First-principles investigations of the electronic, magnetic and thermoelectric properties of VTiRhZ (Z= Al, Ga, In) Quaternary Heusler alloys, *Materials Chemistry and Physics* **278** (2022) 125685, `https://doi.org/10.1016/j.matchemphys.2021.125685`
41. G. Forozani *et al.*, Structural, electronic and magnetic properties of CoZrIrSi quaternary Heusler alloy: First-principles study, *Journal of Alloys and Compounds* **815** (2020) 152449, `https://doi.org/10.1016/j.jallcom.2019.152449`
42. J. Jami *et al.*, First-principles investigation of the structure, stability, and magnetic properties of the Heusler alloy Fe 2 MnSn, *Physical Review B* **108** (2023) 054431, `https://doi.org/10.1103/PhysRevB.108.054431`
43. H. Alqurashi and B. Hamad, Magnetic structure, mechanical stability and thermoelectric properties of VTiRhZ (Z= Si, Ge, Sn) quaternary Heusler alloys: First-principles calculations, *Applied Physics A* **127** (2021) 799, `https://doi.org/10.1007/s00339-021-04949-0`
44. M. Benidris *et al.*, Electronic structure, thermoelectric, mechanical and phonon properties of full-Heusler alloy (Fe 2 CrSb): a first-principles study, *Bulletin of Materials Science* **44** (2021) 1, `https://doi.org/10.1007/s12034-021-02496-1`

45. D. Hoat, Structural, optoelectronic and thermoelectric properties of antiperovskite compounds Ae3PbS (Ae= Ca, Sr and Ba): a first principles study, *Physics Letters A* **383** (2019) 1648, `https://doi.org/10.1016/j.physleta.2019.02.013`

46. P. K. Kamlesh *et al.*, Investigation of inherent properties of XScZ (X= Li, Na, K; Z= C, Si, Ge) half-Heusler compounds: appropriate for photovoltaic and thermoelectric applications, *Physica B: Condensed Matter* **615** (2021) 412536, `https://doi.org/10.1016/j.physb.2020.412536`

47. D. Shrivastava and S. P. Sanyal, Theoretical study of structural, electronic, phonon and thermoelectric properties of KScX (X= Sn and Pb) and KYX (X= Si and Ge) half-Heusler compounds with 8 valence electrons count, *Journal of Alloys and Compounds* **784** (2019) 319, `https://doi.org/10.1016/j.jallcom.2019.01.050`

48. M. Holland, Analysis of lattice thermal conductivity, *Physical review* **132** (1963) 2461, `https://doi.org/10.1103/PhysRev.132.2461`

49. A. Amudhavalli *et al.*, First principles study of structural and optoelectronic properties of Li based half Heusler alloys, *Computational Condensed Matter* **14** (2018) 55, `https://doi.org/10.1016/j.cocom.2018.01.002`

50. P. Larson *et al.*, Electronic structure of rare-earth nickel pnictides: Narrow-gap thermoelectric materials, *Physical Review B* **59** (1999) 15660, `https://doi.org/10.1103/PhysRevB.59.15660`

51. M. Naseri and D. Hoat, First principles investigation on elastic, optoelectronic and thermoelectric properties of KYX (X= Ge, Sn and Pb) half-heusler compounds, *Journal of Molecular Graphics and Modelling* **92** (2019) 249, `https://doi.org/10.1016/j.jmgm.2019.08.002`

52. G. K. Madsen, J. Carrete, and M. J. Verstraete, BoltzTraP2, a program for interpolating band structures and calculating semi-classical transport coefficients, *Computer Physics Communications* **231** (2018) 140, `https://doi.org/10.1016/j.cpc.2018.05.010`

53. C. Han, Z. Li, and S. Dou, Recent progress in thermoelectric materials, *Chinese science bulletin* **59** (2014) 2073, `https://doi.org/10.1007/s11434-014-0237-2`

54. B. Anissa, D. Radouan, and I. K. Durukan, Study of structural, electronic, elastic, optical and thermoelectric properties of half-Heusler compound RbScSn: A TB-mBJ DFT study, *Optical and Quantum Electronics* **54** (2022) 372, `https://doi.org/10.1007/s11082-022-03780-y`

55. J. Zhang *et al.*, Phosphorene nanoribbon as a promising candidate for thermoelectric applications, *Scientific reports* **4** (2014) 6452, `https://doi.org/10.1038/srep06452`

56. N. Chami *et al.*, Computational prediction of structural, electronic, elastic, and thermoelectric properties of FeV X (X= as, P) half-heusler compounds, *Journal of Electronic Materials* **49** (2020) 4916, `https://doi.org/10.1007/s11664-020-08225-4`

57. A. Reshak and S. Auluck, Thermoelectric properties of nowotny-juza NaZnX (X= P, as and Sb) compounds, *Computational Materials Science* **96** (2015) 90, `https://doi.org/10.1016/j.commatsci.2014.09.008`

58. M.-S. Lee, F. P. Poudeu, and S. Mahanti, Electronic structure and thermoelectric properties of Sb-based semiconducting half-Heusler compounds, *Physical Review B-Condensed Matter and Materials Physics* **83** (2011) 085204, `https://doi.org/10.1103/PhysRevB.83.085204`

59. M. K. Yadav and B. Sanyal, First-principles study of thermoelectric properties of CuI, *Materials Research Express* **1** (2014) 015708, `https://doi.org/10.1088/2053-1591/1/1/015708`

60. D. J. Singh, Doping-dependent thermopower of PbTe from Boltzmann transport calculations, *Physical Review B-Condensed Matter and Materials Physics* **81** (2010) 195217, `https://doi.org/10.1103/PhysRevB.81.195217`

61. G. A. Slack, The thermal conductivity of nonmetallic crystals, *Solid state physics* **34** (1979) 1, `https://doi.org/10.1016/S0081-1947(08)60359-8`

62. R. Farris *et al.*, Giant thermoelectric figure of merit in multivalley high-complexity-factor LaSO, *Physical Review Materials* **5** (2021) 125406, `https://doi.org/10.1103/PhysRevMaterials.5.125406`

63. J. Kangsabanik, A. Alam *et al.*, Bismuth based half-Heusler alloys with giant thermoelectric figures of merit, *Journal of Materials Chemistry A* **5** (2017) 6131, `https://doi.org/10.1039/C7TA00920H`

64. S. Guo *et al.*, Prediction of improved thermoelectric performance by ordering in double half-Heusler materials, *Journal of Materials Chemistry A* **8** (2020) 23590, `https://doi.org/10.1039/D0TA08364J`